

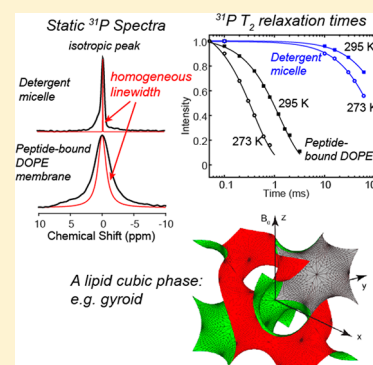
Distinguishing Bicontinuous Lipid Cubic Phases from Isotropic Membrane Morphologies Using ^{31}P Solid-State NMR Spectroscopy

Yu Yang, Hongwei Yao, and Mei Hong*

Department of Chemistry, Massachusetts Institute of Technology, 170 Albany Street, Cambridge, Massachusetts 02139, United States

Supporting Information

ABSTRACT: Nonlamellar lipid membranes are frequently induced by proteins that fuse, bend, and cut membranes. Understanding the mechanism of action of these proteins requires the elucidation of the membrane morphologies that they induce. While hexagonal phases and lamellar phases are readily identified by their characteristic solid-state NMR line shapes, bicontinuous lipid cubic phases are more difficult to discern, since the static NMR spectra of cubic-phase lipids consist of an isotropic ^{31}P or ^2H peak, indistinguishable from the spectra of isotropic membrane morphologies such as micelles and small vesicles. To date, small-angle X-ray scattering is the only method to identify bicontinuous lipid cubic phases. To explore unique NMR signatures of lipid cubic phases, we first describe the orientation distribution of lipid molecules in cubic phases and simulate the static ^{31}P chemical shift line shapes of oriented cubic-phase membranes in the limit of slow lateral diffusion. We then show that ^{31}P T_2 relaxation times differ significantly between isotropic micelles and cubic-phase membranes: the latter exhibit 2 orders of magnitude shorter T_2 relaxation times. These differences are explained by the different time scales of lipid lateral diffusion on the cubic-phase surface versus the time scales of micelle tumbling. Using this relaxation NMR approach, we investigated a DOPE membrane containing the transmembrane domain (TMD) of a viral fusion protein. The static ^{31}P spectrum of DOPE shows an isotropic peak, whose T_2 relaxation times correspond to that of a cubic phase. Thus, the viral fusion protein TMD induces negative Gaussian curvature, which is an intrinsic characteristic of cubic phases, to the DOPE membrane. This curvature induction has important implications to the mechanism of virus–cell fusion. This study establishes a simple NMR diagnostic probe of lipid cubic phases, which is expected to be useful for studying many protein-induced membrane remodeling phenomena in biology.



INTRODUCTION

Nonlamellar lipid membranes with high curvature are generated during many protein-mediated biological processes such as virus–cell fusion, virus budding, endocytosis, and pore formation by lytic and antimicrobial peptides.^{1–5} Characterizing the type of membrane curvatures is important for understanding the mechanism of action of these proteins. Because lipid membranes are inherently noncrystalline and dynamic, solid-state NMR (SSNMR) spectroscopy is a natural technique for their characterization.

Liquid-crystalline phases formed by surfactants and lipids have been well studied by a variety of techniques (see, e.g. ref 6). The lamellar phase and the hexagonal phases give rise to characteristic static ^{31}P NMR spectral line shapes that allow these phases to be identified readily. However, among nonlamellar membrane morphologies, several types give rise to an isotropic peak in the static NMR spectra. These morphologies include micelles, small unilamellar vesicles, and cubic phases.^{7,8} Bicontinuous lipid cubic phases have received increasing attention in recent years because of the importance of this class of topological structures for membrane fusion, membrane scission, virus budding, and pore formation. Bicontinuous cubic phases are periodic repeats of minimal surfaces on which every point has negative Gaussian curvature

and zero mean curvature.^{9–11} The Gaussian curvature is the product of two principal curvatures at a point, while the mean curvature is the average. Thus, every point on the surface of bicontinuous cubic phases has equal magnitudes of positive and negative principal curvatures. Based on crystallographic space groups and symmetries, three bicontinuous lipid cubic phases can be distinguished: $Pn3m$ (also called double diamond or D surface), $Ia3d$ (gyroid or G surface), and $Im3m$ (primitive or P surface).^{12,13} A lipid bilayer drapes onto the minimal surface, the two sides of which lie a continuous region of water. Bicontinuous cubic phases separate water into two non-intersecting channels. For the $Im3m$ (P), $Pn3m$ (D), and $Ia3d$ (G) phases, water channels meet at 6-way (90°), 4-way (109.5°), and 3-way (120°) junctions, respectively (Figure 1).

Bicontinuous lipid cubic phases commonly exhibit unit-cell dimensions of 10–20 nm, which are not much larger than the dimensions of micelles. Thus, lipid lateral diffusion on cubic-phase surfaces causes fast molecular reorientation. Because of the symmetry of these phases, this fast reorientation averages second-rank nuclear-spin interaction tensors to their isotropic

Received: January 30, 2015

Revised: March 27, 2015

Published: March 27, 2015

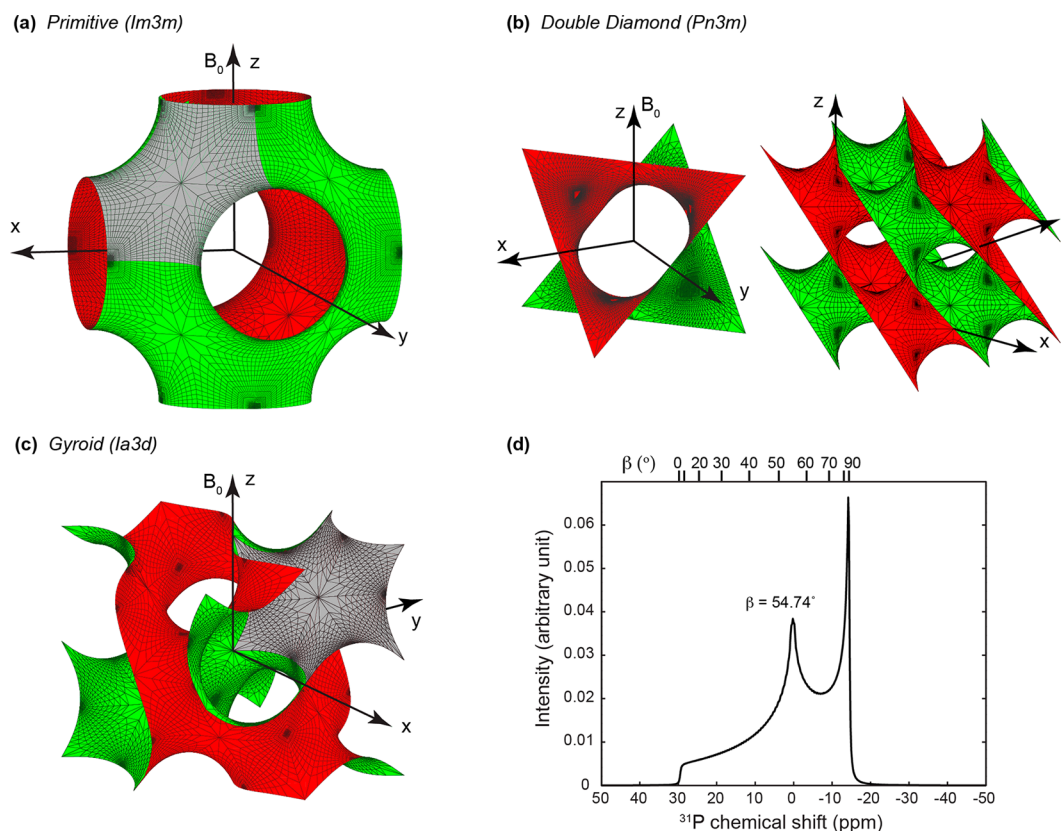


Figure 1. Geometries of three common bicontinuous cubic phases and the calculated quasi-static ^{31}P NMR line shape for an oriented cubic-phase membrane. Red and green colors denote the two surfaces of the bilayer. (a) The primitive $Im\bar{3}m$ phase. (b) The double diamond $Pn\bar{3}m$ phase. For clarity, an extended view containing 8 unit cells is shown on the right at a different angle. (c) The gyroid $Ia\bar{3}d$ phase. Because of symmetry, a saddle area is shown in gray in (a) and (c) to indicate the minimum surface used for calculating the ^{31}P NMR line shape. (d) Simulated ^{31}P CSA line shape of the three cubic phases, assuming an oriented cubic-phase membrane whose z -axis of the unit cell is parallel to the magnetic field. All three cubic phases give the same spectrum.

values.⁷ Thus, although bicontinuous cubic phases are structurally not isotropic, their static solid-state NMR spectra exhibit an “isotropic” peak, indistinguishable from the spectra of truly isotropic membrane morphologies such as micelles and small vesicles. Here the term “isotropic peak” refers to a peak at the isotropic NMR frequency, while “isotropic” morphologies refer to the three-dimensional structures of micelles and small vesicles.

Although isotropic phases and cubic phases cannot be distinguished by static NMR line shapes, they may be resolved by NMR relaxation times. In contrast to NMR line shapes, whose averaging depends only on the lower limit of motional rates, relaxation times are sensitive to motions on a range of time scales. In lipid membranes, many molecular motions exist to drive nuclear-spin relaxation. These include segmental torsional motions, whole-body uniaxial rotational diffusion around the long molecular axis, wobble of the molecular axis in a cone, tumbling of vesicles or micelles, and lipid lateral diffusion on the membrane surface.^{14,15} The torsional motions, uniaxial rotation, and wobble typically occur on the picosecond to nanosecond time scales for hydrated membranes.^{16,17} Tumbling of nanometer-sized vesicles and micelles occurs on the microsecond time scale. Lateral diffusion depends on the radius of curvature and the diffusion coefficient. For nanometer-sized vesicles or micelles, lateral diffusion occurs on the tens of microsecond time scale, whereas for ~ 100 nm or larger vesicles, lateral diffusion occurs on the millisecond time scale.

Thus, tumbling and lateral diffusion are much slower than torsional motions and rotational diffusion.

While a large body of literature exists on using ^{31}P , ^2H , ^{13}C , and ^{14}N relaxation NMR to investigate lipid motions in lamellar membranes (see, e.g. refs 18 and 19), the application of relaxation NMR for studying nonlamellar membrane morphologies is more scarce. ^2H and ^{14}N relaxation NMR has been used to study surfactant motions in various liquid-crystalline phases.^{20–22} ^{13}C T_2 relaxation has been used to measure lateral diffusion coefficients of lipids in sonicated and extruded small vesicles.²³ ^{31}P and ^2H relaxation NMR has been used to compare the curvatures of hexagonal and lamellar phases²⁴ and motions in spherical supported vesicles versus multilamellar vesicles.²⁵ Halle and co-workers presented a theory of nuclear-spin relaxation in bicontinuous cubic-phase liquid crystals that suggested the possibility of extracting time correlation functions for different cubic phases.²⁶ However, to our knowledge, no experimental demonstration of relaxation NMR for distinguishing cubic phases from isotropic phases has been reported.

In this work, we show that ^{31}P T_2 relaxation times readily distinguish lipid isotropic phases and bicontinuous cubic phases. We use LMPC as a representative micelle and monoolein/POPC as a representative cubic-phase membrane. From their ^{31}P T_1 and T_2 relaxation times, we extract correlation times of fast and slow motions and compare them between the micelle and the cubic-phase samples. On the basis of these model-compound data, we investigate the ^{31}P relaxation times of a DOPE membrane containing the

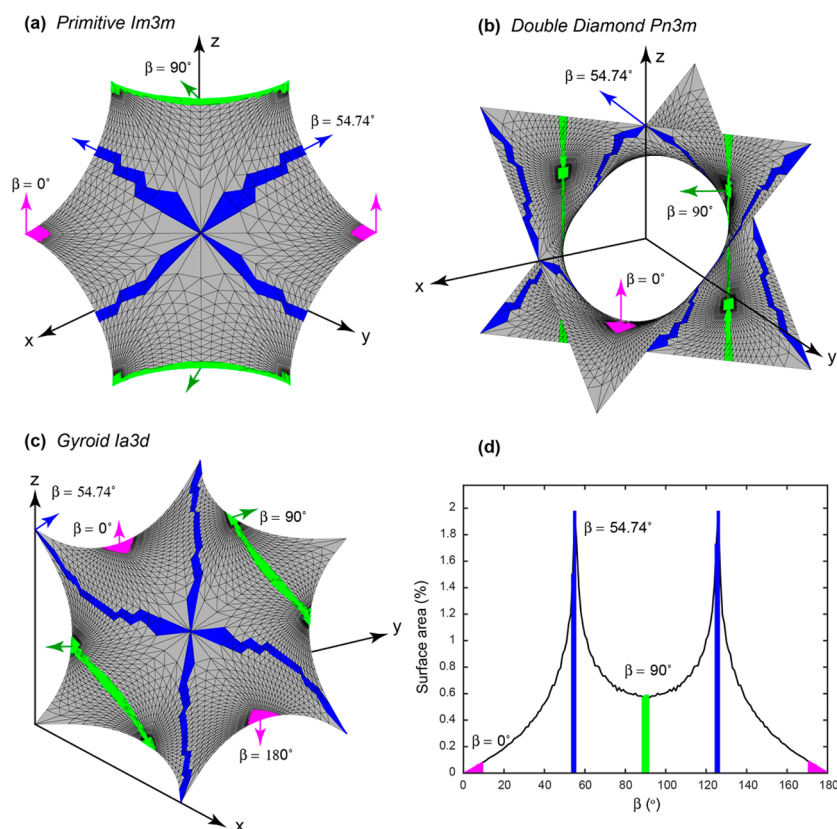


Figure 2. Distribution of the angle β between the local bilayer normal and the z -axis of the cubic-phase unit cell. (a) One saddle of the primitive surface $Im3m$. (b) One unit of the double diamond surface $Pn3m$. (c) One saddle of the gyroid surface $Ia3d$. Green, magenta, and blue areas denote β angles of 90° , 0° or 180° , and 54.7° or 125.3° , respectively. (d) Normalized surface area as a function of the β angle. The smallest surface areas occur at $\beta = 0^\circ$ and 180° , while $\beta = 54.7^\circ$ and 125.3° exhibit the largest surface area.

transmembrane domain (TMD) of a viral fusion protein. This viral fusion TMD causes an isotropic ^{31}P peak to the DOPE membrane. We show that the ^{31}P T_2 relaxation times of this TMD-bound DOPE membrane are diagnostic of a cubic phase, which has significant implications to the mechanism of virus-cell fusion. We also examine the temperature dependences of the ^{31}P relaxation times for all three membranes to obtain activation energies of fast and slow motions. In addition, we provide a mathematical description of the orientation distribution of lipids in cubic phases and show that, in the limit of slow lateral diffusion, an oriented cubic-phase membrane has unique NMR line shapes.

MATERIALS AND METHODS

Membrane Sample Preparation. Three membrane samples were prepared: 1-myristoyl-2-hydroxy-*sn*-glycero-3-phosphocholine (LMPC), 1-monoolein (MO)/1-palmitoyl-2-oleoyl-*sn*-glycero-3-phosphocholine (POPC) (17:3), and 1,2-dioleoyl-*sn*-glycero-3-phosphoethanolamine (DOPE) membrane containing the TMD of the parainfluenza virus 5 (PIV5) F protein. The peptide:lipid molar ratio of the TMD/DOPE sample is 1:15. LMPC was dissolved in water to a concentration of 400 mM and transferred into a 4 mm magic-angle-spinning (MAS) rotor. MO and POPC were codissolved in chloroform, while the PIV5 TMD and DOPE were dissolved in TFE and chloroform, respectively. The organic solvents were removed by nitrogen gas, and the mixtures were lyophilized. The dry powders were suspended in 4 mL of pH 7.5 HEPES buffer (10 mM HEPES-NaOH, 1 mM EDTA, and 1 mM

NaN_3). The MO/POPC mixture was incubated at 4°C overnight, while the TMD/DOPE mixture was dialyzed against 1 L buffer for 1 day. The samples were centrifuged at 4°C and 55 000 rpm for 3 h to obtain membrane pellets, which were equilibrated to $\sim 55\%$ hydration for MO/POPC and $\sim 30\%$ for TMD/DOPE before transfer into MAS rotors.

Solid-State NMR Experiments. Static ^{31}P NMR experiments were carried out on a Bruker 400 MHz (9.4 T) spectrometer operating at Larmor frequencies of 400.49 MHz for ^1H and 162.12 MHz for ^{31}P . ^{31}P T_2 relaxation times were measured between 273 and 295 K using a Hahn echo sequence ($90^\circ - \tau - 180^\circ - \tau$) under 30 kHz ^1H decoupling and echo delays (τ) of 50 μs –30 ms. To extract T_2 values, echo intensities as a function of 2τ were fit to a single-exponential function $Ae^{-2\tau/T_2}$, where A is close to 1. ^{31}P T_1 relaxation times were measured using the inversion recovery sequence ($180^\circ - \tau - 90^\circ$). The intensities was fit to a single-exponential function $B(1 - Ce^{-\tau/T_1})$, where $B = 1$ and $C = 2$ in the ideal case but are slightly adjustable in the fitting.

RESULTS

Anisotropic NMR Line Shapes of Cubic-Phase Membranes. In static solid-state NMR spectra, cubic-phase membranes exhibit a narrow peak at the isotropic frequency because of fast lateral diffusion over the highly curved surface of the membrane. This isotropic spectrum is identical to that of micelles and small vesicles, even though the molecular orientational distribution in the cubic phase is anisotropic. To elucidate this orientation distribution, we simulate the quasi-

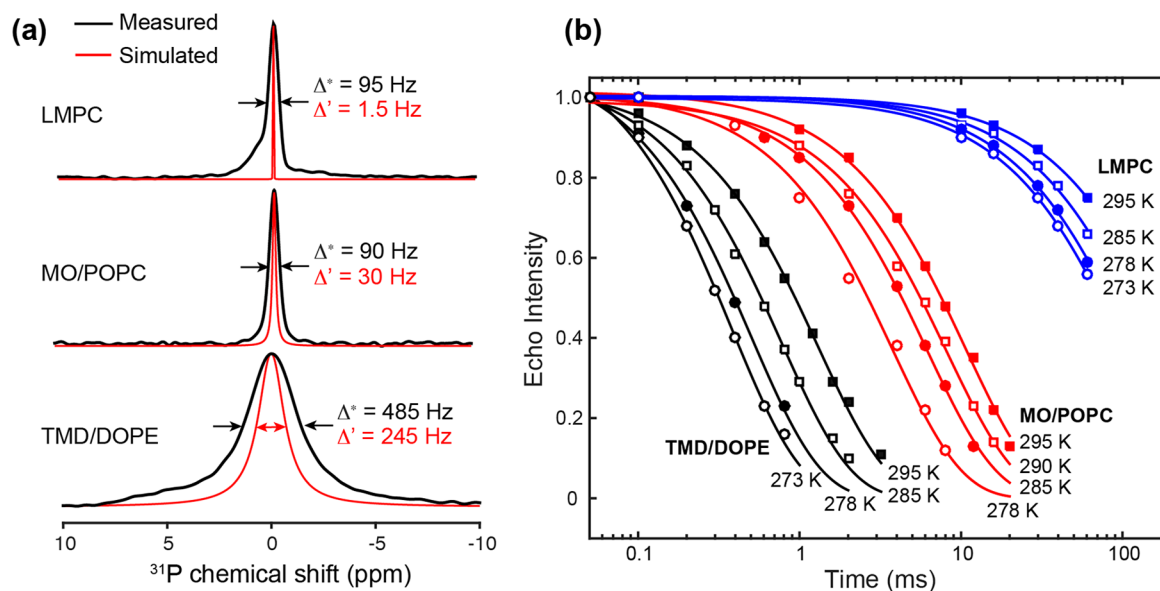


Figure 3. ^{31}P T_2 relaxation times of LMPC, MO/POPC, and TMD-bound DOPE membranes. (a) Static ^{31}P spectra of the three samples at 295 K. The measured spectra with apparent line widths Δ^* are shown in black whereas simulated Lorentzian line shapes with homogeneous line widths Δ' based on the ^{31}P T_2 are shown in red. (b) ^{31}P spin-echo intensities as a function of echo delay from 273 to 295 K. LMPC micelles have ^{31}P T_2 values of 104–207 ms and MO/POPC shows T_2 's of 3.7–10.7 ms, while the TMD/DOPE sample shows the shortest ^{31}P T_2 values of 0.38–1.3 ms.

Table 1. ^{31}P T_2 Relaxation Times (ms) of LMPC, MO/POPC, and TMD/DOPE Membranes

membrane	273 K	278 K	285 K	290 K	295 K
LMPC	104 ± 4	117 ± 7	150 ± 18		207 ± 11
MO/POPC		3.7 ± 0.5	6.1 ± 0.2	8.2 ± 0.6	10.7 ± 0.5
TMD/DOPE	0.38 ± 0.02	0.50 ± 0.03	0.77 ± 0.04		1.3 ± 0.05

static ^{31}P NMR line shapes of oriented cubic-phase membranes in the absence of lateral diffusion. If the cubic phases are randomly oriented, then the NMR line shape reverts to the powder line shape of unoriented bilayers.

In liquid-crystalline lipid membranes, the three principal values of the rigid-limit ^{31}P chemical shielding tensor, σ_{xx} , σ_{yy} , and σ_{zz} , are averaged by the uniaxial rotation of the phospholipids to two components, σ_{\parallel} and σ_{\perp} , where σ_{\parallel} is the component parallel to the uniaxial rotational axis, which is the local bilayer normal, while σ_{\perp} is the component perpendicular to it. The asymmetry parameter of the chemical shielding tensor, $\eta \equiv (\sigma_{yy} - \sigma_{xx})/(\sigma_{zz} - \sigma_{\text{iso}})$, is averaged to 0, $\bar{\eta} = 0$, while the averaged anisotropy parameter, $\bar{\delta} \equiv 2/3(\sigma_{\parallel} - \sigma_{\perp})$, is ~ 30 ppm for most phospholipids.

The angle β between the magnetic field B_0 and the local bilayer normal gives the orientation-dependent ^{31}P chemical shift frequency:

$$\omega_{\text{cs}}(\beta) = \omega_{\text{iso}} + \frac{1}{2}\bar{\delta}(3\cos^2\beta - 1) \quad (1)$$

where ω_{iso} is the trace of the chemical shift tensor. The Euler rotations that relate the laboratory frame to the bilayer frame are most conveniently considered through a coordinate system fixed to the cubic-phase crystal frame. When B_0 is coincident with the z -axis of this crystal frame (Figure 1a–c), β is simply the polar angle of the local bilayer normal in the crystal frame. Thus, based on the distribution of β on the cubic-phase surface, we can calculate the ^{31}P NMR line shape. The line shapes of other B_0 orientations relative to the crystal frame can be similarly calculated, as we show in the Supporting Information.

We constructed the geometries of the three bicontinuous cubic phases (Figure 1a–c) following the mathematical protocols of Klinowski^{27–29} and Finch.^{30,31} Detailed equations are given in the Supporting Information. For symmetry reasons, only 1/8 of the unit cells of the primitive ($Im3m$) and gyroid ($Ia3d$) surfaces need to be sampled to obtain the line shapes of the full unit cell (Figures S1–S3). The CSA spectrum for B_0 along the z -axis of the unit cell is a superposition of an isotropic peak with an $\bar{\eta} = 0$ powder line shape and is identical for the three cubic phases (Figure 1d). Thus, the cubic-phase spectrum differs from the lamellar bilayer spectrum at the isotropic frequency. Since this isotropic frequency corresponds to bilayer normals that are oriented at the magic angle, 54.7° , from the magnetic field, to show the high population of this magic-angle orientation, we plot the β distribution for the three cubic phases (Figure 2). Indeed, the surface area at 54.7° and 125.3° dominates that of any other angles, and the distribution function can be approximated by the sum of $\sin\beta$ and additional intensity at the magic angle. The CSA line shape when B_0 points along the x - and y -axes of the crystal frame is identical with Figure 1d (simulation not shown), but other B_0 orientations have distinct line shapes, some of which are given in the Supporting Information (Figure S4).

While these simulated static ^{31}P CSA line shapes are interesting, in practice it is challenging to suppress lipid lateral diffusion and produce oriented cubic-phase membranes. Thus, we next explore ^{31}P relaxation NMR to identify cubic phases under the realistic situation of random orientation and in the presence of fast lateral diffusion.

^{31}P Relaxation Times of Micelles versus Cubic-Phase Membranes. The static ^{31}P spectra of LMPC, MO/POPC,

Table 2. ^{31}P T_1 Relaxation Times (s) of LMPC, MO/POPC, and TMD/DOPE Membranes

membrane	273 K	278 K	285 K	290 K	295 K
LMPC	0.81 ± 0.01	0.82 ± 0.01	0.88 ± 0.01		1.06 ± 0.03
MO/POPC		0.74 ± 0.02	0.81 ± 0.02	0.88 ± 0.03	0.95 ± 0.03
TMD/DOPE	1.13 ± 0.02	1.09 ± 0.03	1.01 ± 0.02		0.99 ± 0.02

and TMD/DOPE membranes are shown in Figure 3a. All three samples exhibit a single ^{31}P isotropic peak at ambient temperature. The full widths at half-maximum, Δ^* , are ~ 90 Hz for LMPC and MO/POPC and increase to ~ 485 Hz for DOPE. In contrast, the ^{31}P T_2 relaxation decays of the three membranes, plotted on a logarithmic time scale (Figure 3b), show a 2 orders of magnitude difference among the three samples: the LMPC micelle has T_2 values of more than 100 ms between 275 and 295 K, while the TMD/DOPE membrane shows ^{31}P T_2 's of 0.3–1.3 ms (Table 1). POPC in the cubic-phase MO/POPC membrane has intermediate T_2 's of several milliseconds. All three samples exhibit increasing T_2 with temperature. These T_2 values translate to homogeneous line widths, $\Delta' \equiv 1/\pi T_2$, of 1.5 Hz for LMPC, 30 Hz for MO/POPC, and 245 Hz for TMD/DOPE at ambient temperature. Simulated Lorentzian line shapes for these homogeneous line widths are shown in Figure 3a to compare with the observed apparent line widths. It can be seen that although the LMPC sample has the narrowest apparent line width, it is more inhomogeneously broadened (i.e., large Δ^*/Δ') than MO/POPC and TMD/DOPE, suggesting that the micelles have a large distribution of sizes, while the TMD/DOPE spectrum is the most homogeneously broadened.

Compared to T_2 , ^{31}P T_1 relaxation times are more uniform among the three samples, about 1 s at ambient temperature (Table 2 and Figure 4). However, LMPC and MO/POPC

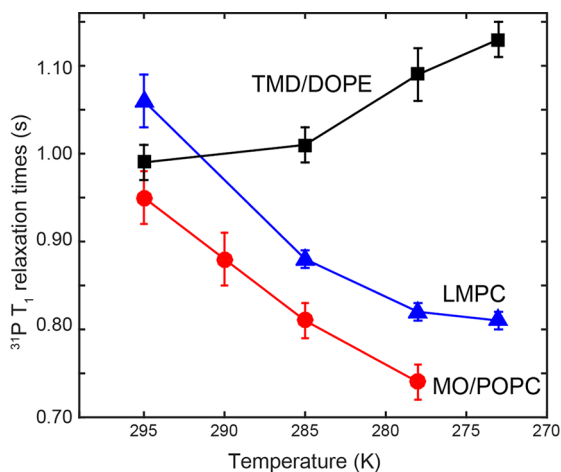


Figure 4. ^{31}P T_1 relaxation times of LMPC, MO/POPC and TMD/DOPE membranes as a function of temperature. The T_1 values increase with temperature for LMPC and MO/POPC and decrease with temperature for TMD/DOPE.

show decreasing T_1 with decreasing temperature while TMD/DOPE manifests the opposite trend. Thus, the nanosecond motions in the TMD/DOPE membrane occur on the slow side of the T_1 minimum while those in the MO/POPC and LMPC membranes occur on the fast side (see below).

We now consider the mechanisms of ^{31}P T_1 and T_2 relaxations in lipid membranes in order to extract motional correlation times for the three membranes. The nuclear-spin

interactions relevant for ^{31}P relaxation are the ^{31}P CSA and ^{31}P – ^1H dipole coupling. At the magnetic field of 9.4 T used here, the CSA mechanism dominates, and the T_1 and T_2 relaxation rates can be expressed as^{32,33}

$$R_1^{\text{CSA}} = \frac{2}{15} \omega_p^2 \sigma^2 \left(1 + \frac{\eta^2}{3} \right) J(\omega_p) \quad (2)$$

$$R_2^{\text{CSA}} = \frac{1}{15} \omega_p^2 \sigma^2 \left(1 + \frac{\eta^2}{3} \right) \left[J(\omega_p) + \frac{4}{3} J(0) \right] \quad (3)$$

where ω_p is the ^{31}P Larmor frequency, $\sigma \equiv \frac{3}{2}(\sigma_{zz} - \sigma_{\text{iso}})$ is the rigid-limit chemical shift anisotropy, and $J(\omega)$ is the spectral density at frequency ω and is the Fourier transform of the correlation function of motion. If the motion is Markovian (e.g., diffusive or jumplike), then the correlation function is exponential with a time constant τ_c and $J(\omega)$ is Lorentzian:³⁴

$$J(\omega) = \frac{\tau_c}{1 + (\omega\tau_c)^2} \quad (4)$$

To simplify analysis, we separate lipid motions into two types: fast motions with a correlation time τ_f and slow overall motions with a correlation times τ_s . With this approximation, the spectral density function becomes^{35,36}

$$J(\omega; \tau_s, \tau_f) = \frac{S^2 \tau_s}{1 + (\omega\tau_s)^2} + \frac{(1 - S^2) \tau_f}{1 + (\omega\tau_f)^2} \quad (5)$$

where S is the order parameter of the fast motion.

The rigid-limit ^{31}P CSA (σ) is about 160 ppm, η is about 0.57,^{16,37} and the Larmor frequency in our experiments is $\omega_p = 2\pi \times 162 \times 10^6$ rad/s. The order parameters of the glycerol backbone and the beginning of the headgroup are ~ 0.2 based on measured C–H dipolar couplings and ^{31}P and ^{13}C CSAs in liquid-crystalline phosphocholine.^{38,39} Thus, from the measured T_1 and T_2 values, we can extract the two unknowns, τ_f and τ_s , by solving the simultaneous eqs 2 and 3. In principle, from these quadratic equations more than one solution of τ_f and τ_s is possible. However, by removing unphysical values and using the fact that τ_f and τ_s should decrease with increasing temperature, we can obtain a unique set of correlation times at each temperature.

Tables 3 lists the measured fast and slow correlation times for the three membranes at various temperatures. We found τ_f values of 0.27–0.43 ns for LMPC and MO/POPC but a 10–

Table 3. Fast and Slow Correlation Times of Three Membranes at Different Temperatures

membrane		273 K	278 K	285 K	290 K	295 K
LMPC	τ_f (ns)	0.38	0.37	0.34		0.27
	τ_s (μs)	0.077	0.067	0.050		0.035
MO/POPC	τ_f (ns)		0.43	0.38	0.34	0.31
	τ_s (μs)		2.5	1.5	1.2	0.89
TMD/DOPE	τ_f (ns)	3.9	3.7	3.4		3.3
	τ_s (μs)	25	19	12		7.3

fold longer τ_f value of 3–4 ns for the TMD/DOPE sample. Thus, phosphocholines in the micelle and the cubic-phase monoolein undergo faster motions than DOPE lipids in complex with the fusion protein TMD. The longer correlation time of DOPE may result from intermolecular hydrogen bonding between phosphoethanolamine headgroups and from DOPE–TMD interactions.

For slow motions, the τ_s values differ by 2 orders of magnitude among the three membranes (Table 3). LMPC has τ_s values of 0.04–0.08 μ s over the temperature range studied, while POPC in cubic-phase MO/POPC exhibits τ_s values of 0.9–2.5 μ s. TMD-bound DOPE has the longest τ_s of 7.3–25 μ s.

To understand the origin of these very different τ_s values, we estimate the correlation times of various slow motions in lipid membranes. Two main sources of slow motions are whole-body tumbling and lipid lateral diffusion, whose correlation times can be calculated as⁴⁰

$$\frac{1}{\tau_s} = \frac{1}{\tau_s^d} + \frac{1}{\tau_s^t} = \left(\frac{r_L^2}{6D_L} \right)^{-1} + \left(\frac{4\pi r_t^3 \eta_W}{3kT} \right)^{-1} \quad (6)$$

where τ_s^d is the correlation time for lipid lateral diffusion, τ_s^t is the correlation time for tumbling, D_L is the lateral diffusion coefficient, r_L is the radius of curvature for lateral diffusion, r_t is the radius of the tumbling vesicle, T is the absolute temperature, k is the Boltzmann constant, and η_W is the viscosity of the aqueous solution. For lipid cubic phases, $r_L \ll r_t$ because of the extended nature of the cubic-phase assembly; thus, τ_s^d is much shorter than τ_s^t , making lateral diffusion the determining factor for the overall τ_s . Using a typical D_L value of 10^{-8} cm²/s and a radius of 10 nm, we estimate a τ_s value of ~ 17 μ s when lateral diffusion dominates the slow motion. For micelles, $r_L = r_t$. Using an η_W of 0.891×10^{-3} kg/(m s), a radius of 5 nm, and T of 295 K, we estimate a tumbling correlation time τ_s^t of 0.13 μ s, which is much shorter than τ_s^d and thus dominates τ_s . Thus, micelles should have 2 orders of magnitude shorter τ_s than lipid cubic phases, consistent with the measured τ_s differences between LMPC and MO/POPC. Therefore, the fact that TMD/DOPE exhibits longer τ_s assigns this membrane to the cubic phase.

We can extract the activation energies E_a of the fast and slow motions from the measured temperature dependence of the correlation times. Assuming Arrhenius behavior, the correlation time depends on T as

$$\tau = \tau_0 e^{E_a/RT} \quad (7)$$

where R is the ideal gas constant. Figure 5 plots $\ln(\tau)$ as a function of $1000/T$, the slope of which gives the activation energies. For fast motions, we found similar activation energies of 13–14 kJ/mol for LMPC and MO/POPC, while the TMD/DOPE membrane has a 3-fold lower activation energy of 5.2 kJ/mol. For slow motions, activation energies of 26–41 kJ/mol were found, with LMPC giving the smallest value while MO/POPC and TMD/DOPE exhibit larger and similar activation energies.

DISCUSSION

These ³¹P relaxation data reveal that cubic-phase membranes can be distinguished from isotropic micelles by their different T_2 relaxation times or homogeneous line widths. Although LMPC and MO/POPC have the same apparent ³¹P line widths

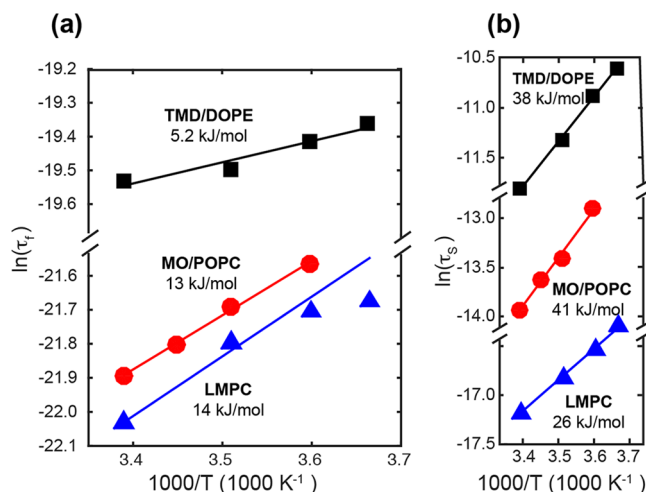


Figure 5. Activation energies of slow and fast motions in the three lipid membranes, extracted from the slope of the correlation times with respect to inverse temperature. (a) $\ln(\tau_f)$ as a function of temperature. The activation energies range from 5.2 to 14 kJ/mol. (b) $\ln(\tau_s)$ as a function of temperature. The activation energies range from 26 to 41 kJ/mol.

(Figure 3a), the underlying homogeneous line widths are dramatically different. The narrower homogeneous line width of the LMPC micelle is empirically consistent with the fluid nature of the micelle sample. The estimated correlation times for whole-body tumbling and lateral diffusion over a radius of 5–10 nm provide insights into the different orders of magnitude of T_2 relaxation times. To understand τ_s and τ_f 's contribution to ³¹P T_2 and T_1 relaxation times, we consider the dependences of the spectral density function on correlation times. Setting τ_f to 0.1–10 ns and τ_s to 10 ns–100 μ s, the spectral density at the Larmor frequency, $J(\omega_p; \tau_s, \tau_f)$, depends on τ_s and τ_f as

$$\frac{\partial J(\omega_p; \tau_s, \tau_f)}{\partial \tau_s} = S^2 \frac{1 - (\omega_p \tau_s)^2}{[1 + (\omega_p \tau_s)^2]^2} \approx -\frac{S^2}{(\omega_p \tau_s)^2} \quad (8)$$

$$\frac{\partial J(\omega_p; \tau_s, \tau_f)}{\partial \tau_f} = (1 - S^2) \frac{1 - (\omega_p \tau_f)^2}{[1 + (\omega_p \tau_f)^2]^2} \quad (9)$$

The approximation in eq 8 results from the fact that $(\omega_p \tau_s)^2 \gg 1$. Since S is ~ 0.2 , $J(\omega_p; \tau_s, \tau_f)$ has negligible dependence on τ_s , indicating that slow motion has little impact on T_1 . In contrast, since $\omega_p \tau_f \sim 1$, τ_f has a significant effect on $J(\omega_p; \tau_s, \tau_f)$. These dependences of $J(\omega_p; \tau_s, \tau_f)$ are plotted in Figure 6a. Around the T_1 minimum $\tau_f = 1/\omega_p$, T_1 decreases with increasing τ_f when $\tau_f < 1/\omega_p$ but increases with increasing τ_f when $\tau_f > 1/\omega_p$ (Figure 6b).

T_2 relaxation times depend on spectral densities at both the Larmor frequency and $\omega = 0$. From eq 5, $J(0) = S^2 \tau_s + (1 - S^2) \tau_f$, indicating that $J(0)$ is proportional to both τ_f and τ_s . Figure 6c plots the calculated T_2 values as a function of τ_s for several τ_f values. When $\tau_s > 1 \mu$ s, T_2 is dominated by τ_s and mostly independent of τ_f . In this regime, R_2 can be simplified as

$$R_2^{\text{CSA}} \approx \frac{1}{15} \omega_p^2 \sigma^2 \left(1 + \frac{\eta^2}{3} \right) \left(\frac{4}{3} S^2 \tau_s \right) \quad (10)$$

indicating that the T_2 relaxation time is dominated by and inversely proportional to τ_s (Figure 6c). As a result, tumbling micelles with shorter τ_s values ($< 0.1 \mu$ s) have longer T_2

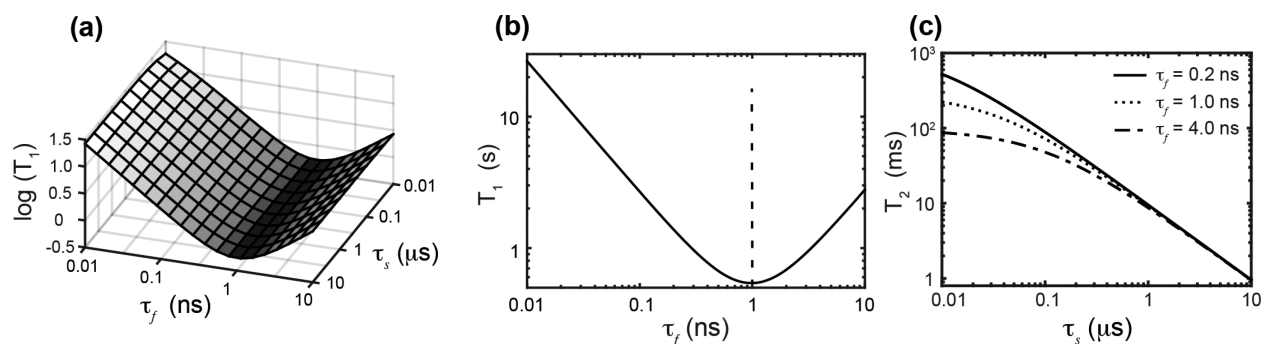


Figure 6. Dependences of ^{31}P T_1 and T_2 relaxation times on fast and slow correlation times τ_f and τ_s . (a) $\log(T_1)$ versus τ_f and τ_s . In the range of $10\text{ ns} < \tau_s < 10\text{ }\mu\text{s}$, T_1 is insensitive to τ_s . (b) ^{31}P T_1 relaxation time as a function of τ_f when $\tau_s = 1\text{ }\mu\text{s}$. Under our experimental condition T_1 has a minimum of $\sim 0.54\text{ s}$, which is achieved when $\tau_f = 1/\omega_p \approx 1\text{ ns}$. (c) ^{31}P T_2 relaxation time as a function of τ_s while τ_f is 0.2, 1, and 4 ns. T_2 decreases with increasing τ_s and τ_f . The dependence of T_2 on τ_f diminishes with increasing τ_s . When $\tau_s > 1\text{ }\mu\text{s}$, T_2 is independent of τ_f , and the relationship between T_2 and τ_s is approximately linear.

relaxation times than cubic-phase membranes with longer τ_s values ($1\text{--}30\text{ }\mu\text{s}$) due to lateral diffusion. The significant τ_s differences between LMPC micelles and the MO/POPC cubic phase are not manifested in the ^{31}P spectral line shapes because both motions are faster than the averaged ^{31}P CSA of $\sim 5\text{ kHz}$. However, at larger magnetic field strengths, the ^{31}P CSA may become sufficiently large such that the cubic-phase ^{31}P spectrum may no longer be averaged to an isotropic frequency. Higher magnetic fields may also facilitate alignment of the cubic-phase membrane, if the magnetic susceptibility anisotropy of the cubic-phase membrane can be made sufficiently large using dopants such as lanthanide ions, so that the calculated ^{31}P line shapes may become observable.

The measured activation energies give useful insights into the nature of various lipid motions. For slow motions, TMD/DOPE and MO/POPC exhibit an activation energy of $\sim 40\text{ kJ/mol}$, whereas the LMPC micelle has a much smaller activation energy of 26 kJ/mol . Pulsed-field gradient NMR data have yielded the activation energies of lipid lateral diffusion in various membranes. For example, hydrated POPC⁴¹ and MO in cubic-phase MO/water mixtures⁴² were reported to have activation energies of $\sim 30\text{ kJ/mol}$. The good agreement between these literature values and our data for TMD/DOPE and MO/POPC supports the assignment of the slow motion in these samples to lateral diffusion. For fast motions, the activation energies are smaller: LMPC and MO/POPC gave a value of $13\text{--}14\text{ kJ/mol}$ while TMD/DOPE showed the smallest activation energy of 5.2 kJ/mol . The former is in excellent agreement with the values obtained from previous field-dependent ^{31}P T_1 relaxation data, which indicated that most phospholipids have an activation energy of $13.2 \pm 1.9\text{ kJ/mol}$ in the liquid-crystalline phase.^{43,44} This energy barrier was assigned to diffusive motions in a spatially rough potential energy landscape⁴⁴ and is associated with motions with correlation times of several nanoseconds. We found τ_f values of less than 1 ns for the LMPC micelle, which suggests that other motional processes may also be present. Single-field ^{31}P relaxation times as measured here are not sufficient to separate multiple fast motions such as torsional motion, headgroup rotation, and lipid uniaxial rotation;⁴⁵ however, such a detailed separation of motional mechanisms is not the focus of this study. Even with our simplifying assumption of only one fast motion, the good agreement between our activation energies for LMPC and MO/POPC and literature values suggests that

the fast motion can be reasonably assigned to rotational diffusion combined with wobble of the molecular axis.

The ^{31}P T_2 relaxation data indicate that the TMD of the fusion protein F of the parainfluenza virus 5 converts the DOPE membrane to a cubic phase. This is consistent with small-angle X-ray scattering (SAXS) data that showed the formation of an $Ia3d$ cubic phase (unpublished data). Thus, the TMD of this viral fusion protein induces negative Gaussian curvature to the DOPE membrane, the type of curvature that is present in hemifusion intermediates and fusion pores.⁴ The active participation of the TMD to viral fusion may not be restricted to the PIV5 fusion protein but may occur in other viral fusion proteins as well. In addition to fusion proteins, the influenza M2 protein has also been shown to induce an isotropic peak in the ^{31}P NMR spectra⁴⁶ and cubic phases in the SAXS spectra,⁴⁷ and this curvature-inducing ability has been correlated with the membrane-scission function of the M2 protein.⁴⁸ The current ^{31}P relaxation NMR approach should be useful for further characterization of M2-induced membrane restructuring as well as for *de novo* determination of the membrane morphologies with an associated isotropic ^{31}P peak as generated by other proteins.

In conclusion, the lipid membrane morphology can be identified by first measuring the static ^{31}P NMR line shapes. Lamellar and hexagonal phases exhibit unique anisotropic powder patterns while micelles and cubic phase exhibit an isotropic peak. If the latter is found, then nonspinning ^{31}P T_2 relaxation times should be measured. If the T_2 is longer than $\sim 100\text{ ms}$ at room temperature, then the membrane is in an isotropic phase, while T_2 's of less than $\sim 10\text{ ms}$ indicate that the membrane is in a bicontinuous cubic phase. Temperature-dependent T_1 and T_2 relaxation times can be further measured to obtain more detailed information about the correlation times of lipid motion. The slow correlation time is especially distinct between the cubic phases (microseconds) and the micellar phase ($10\text{--}100\text{ ns}$).

■ ASSOCIATED CONTENT

Supporting Information

Detailed mathematical modeling, Tables S1–S3 and Figures S1–S4 of the three bicontinuous cubic phases. This material is available free of charge via the Internet at <http://pubs.acs.org>.

■ AUTHOR INFORMATION

Corresponding Author

*E-mail meihong@mit.edu (M.H.).

Notes

The authors declare no competing financial interest.

■ ACKNOWLEDGMENTS

This work is supported by NIH Grant GM066976 to M.H.

■ REFERENCES

- (1) Harrison, S. C. Viral membrane fusion. *Nature Struct. Mol. Biol.* **2008**, *15*, 690–698.
- (2) McMahon, H. T.; Gallop, J. L. Membrane curvature and mechanisms of dynamic cell membrane remodeling. *Nature* **2005**, *438*, 590–596.
- (3) Schmidt, N.; Mishra, A.; Lai, G. H.; Wong, G. C. Arginine-rich cell-penetrating peptides. *FEBS Lett.* **2010**, *584*, 1806–1813.
- (4) Siegel, D. P. The modified stalk mechanism of lamellar/inverted phase transitions and its implications for membrane fusion. *Biophys. J.* **1999**, *76*, 291–313.
- (5) Chernomordik, L. V.; Kozlov, M. M. Protein-lipid interplay in fusion and fission of biological membranes. *Annu. Rev. Biochem.* **2003**, *72*, 175–207.
- (6) De Kruijff, B.; Cullis, P. R.; Verkleij, A. J.; Hope, M. J.; Van Echteld, C. J. A.; Taraschi, T. F. Lipid polymorphism and membrane function. In *The Enzymes of Biological Membranes*; Springer: Berlin, 1985; pp 131–204.
- (7) Lindblom, G.; Rilfors, L. Cubic phases and isotropic structures formed by membranes lipids - possible biological relevance. *Biochim. Biophys. Acta* **1989**, *988*, 221–256.
- (8) Seddon, J. M.; Robins, J.; Gulik-Krzywicki, T.; Delacroix, H. Inverse micellar phases of phospholipids and glycolipids. *Phys. Chem. Chem. Phys.* **2000**, *2*, 4485–4493.
- (9) Anderson, D. M.; Gruner, S. M.; Leibler, S. Geometrical aspects of the frustration in the cubic phases of lyotropic liquid crystals. *Proc. Natl. Acad. Sci. U. S. A.* **1988**, *85*, 5364–5368.
- (10) Luzzati, V.; Spert, P. A. Polymorphism of lipids. *Nature* **1967**, *215*, 701–704.
- (11) Scriven, L. E. Equilibrium bicontinuous structure. *Nature* **1976**, *263*, 123–125.
- (12) Almsheerqi, Z. A.; Landh, T.; Kohlwein, S. D.; Deng, Y. Cubic membranes: the missing dimension of cell membrane organization. *Int. Rev. Cell Mol. Biol.* **2009**, *274*, 275–342.
- (13) Almsheerqi, Z. A.; Margadant, F.; Deng, Y. The Cubic “Faces” of Biomembranes. In *Advances in Planar Lipid Bilayers and Liposomes*; Aiglic, A., Ed.; Academic Press: New York, 2010; Vol. 12.
- (14) Smith, I. C. P.; Ekiel, I. H. Phosphorus-31 NMR of phospholipids in membranes. In *Phosphorus-31 NMR: Principles and Applications*; Academic Press: New York, 1984; pp 447–474.
- (15) Yeagle, P. L. *The Membranes of Cells*, 2nd ed.; Academic Press: San Diego, CA, 1993.
- (16) Roberts, M. F.; Redfield, A. G. High-resolution 31P field cycling NMR as a probe of phospholipid dynamics. *J. Am. Chem. Soc.* **2004**, *126*, 13765–13777.
- (17) Leftin, A.; Brown, M. F. An NMR database for simulations of membrane dynamics. *Biochim. Biophys. Acta* **2011**, *1808*, 818–839.
- (18) Blume, A.; Rice, D. M.; Wittebort, R. J.; Griffin, R. G. Molecular dynamics and conformation in gel & LC phases of PE bilayers. *Biochemistry* **1982**, *21*, 6220–6230.
- (19) Skarjune, R.; Oldfield, E. Physical studies of cell surface and cell membrane structure determination of phospholipid head group organization by deuterium and phosphorus nuclear magnetic resonance spectroscopy. *Biochemistry* **1979**, *18*, 5903–5909.
- (20) Eriksson, P. O.; Khan, A.; Lindblom, G. Nuclear magnetic resonance studies of motion and structure of cubic liquid crystalline phases. *J. Phys. Chem.* **1982**, *86*, 387–393.
- (21) Söderman, O.; Walderhaug, H.; Henriksson, U.; Stills, P. NMR relaxation in isotropic surfactant systems. A 2H, 13C, and 14N NMR study of the micellar (L1) and cubic (I1) phases in the dodecyltrimethylammonium chloride/water system. *J. Phys. Chem.* **1985**, *89*, 3693–3701.
- (22) Söderman, O.; Olsson, U.; Wong, T. C. An x-ray and NMR study of the cubic phase at low water contents in the dodecyltrimethylammonium chloride/water system. *J. Phys. Chem.* **1989**, *93*, 7474–7478.
- (23) Ellena, J. F.; Lepore, L. S.; Cafiso, D. S. Estimating lipid lateral diffusion in phospholipid vesicles from carbon-13 spin-spin relaxation. *J. Phys. Chem.* **1993**, *97*, 2952–2957.
- (24) Thurmond, R. L.; Lindblom, G.; Brown, M. F. Curvature, order, and dynamics of lipid hexagonal phases studied by deuterium NMR spectroscopy. *Biochemistry* **1993**, *32*, 5394–5410.
- (25) Dolainsky, C.; Möps, A.; Bayerl, T. M. Transverse relaxation in supported and unsupported phospholipid model membranes and the influence of ultraslow motions: A 31P - NMR study. *J. Chem. Phys.* **1993**, *98*, 1712–1720.
- (26) Halle, B.; Ljunggren, S.; Lidin, S. Theory of spin relaxation in bicontinuous cubic liquid crystals. *J. Chem. Phys.* **1992**, *97*, 1401–1415.
- (27) Gandy, P. J. F.; Cvijović, D.; Mackay, A. L.; Klinowski, J. Exact computation of the triply periodic D (‘diamond’) minimal surface. *Chem. Phys. Lett.* **1999**, *314*, 543–551.
- (28) Gandy, P. J. F.; Klinowski, J. Exact computation of the triply periodic G (‘gyroid’) minimal surface. *Chem. Phys. Lett.* **2000**, *321*, 363–371.
- (29) Gandy, P. J. F.; Klinowski, J. Exact computation of the triply periodic Schwarz P minimal surface. *Chem. Phys. Lett.* **2000**, *322*, 579–586.
- (30) Finch, S. R. Computer algebra and elliptic functions, 2013; <http://www.people.fas.harvard.edu/~sfinch/resolve/MinSrf.pdf>.
- (31) Finch, S. R. Partitioning problem, 2013; <http://www.people.fas.harvard.edu/~sfinch/resolve/ge2.pdf>.
- (32) Abragam, A. *The Principles of Nuclear Magnetism*; Oxford: Clarendon, UK, 1961.
- (33) Chang, S. L.; Tjandra, N. Temperature dependence of protein backbone motion from carbonyl 13C and amide 15N NMR relaxation. *J. Magn. Reson.* **2005**, *174*, 43–53.
- (34) Lipari, G.; Szabo, A. Model-free approach to the interpretation of nuclear magnetic resonance relaxation in macromolecules. 1. Theory and range of validity. *J. Am. Chem. Soc.* **1982**, *104*, 4546–4559.
- (35) Kay, L. E.; Torchia, D. A.; Bax, A. Backbone dynamics of proteins as studied by nitrogen-15 inverse detected heteronuclear NMR spectroscopy: application to staphylococcal nuclease. *Biochemistry* **1989**, *28*, 8972–8979.
- (36) Tjandra, N.; Feller, S. E.; Pastor, R. W.; Bax, A. Rotational diffusion anisotropy of human ubiquitin from 15N NMR relaxation. *J. Am. Chem. Soc.* **1995**, *117*, 12562–12566.
- (37) Herzfeld, J.; Griffin, R. G.; Haberkorn, R. A. 31P chemical-shift tensors in barium diethyl phosphate and urea-phosphoric acid: model compounds for phospholipid head-group studies. *Biochemistry* **1978**, *17*, 2711–2718.
- (38) Hong, M.; Schmidt-Rohr, K.; Nanz, D. Study of phospholipid structure by 1H, 13C, and 31P dipolar couplings from 2D NMR. *Biophys. J.* **1995**, *69*, 1939–1950.
- (39) Hong, M.; Schmidt-Rohr, K.; Pines, A. NMR measurement of signs and magnitudes of C-H dipolar couplings in lecithin. *J. Am. Chem. Soc.* **1995**, *117*, 3310–3311.
- (40) Marasinghe, P. A. B.; Buffy, J. J.; Schmidt-Rohr, K.; Hong, M. Membrane curvature change induced by an antimicrobial peptide detected by 31P exchange NMR. *J. Phys. Chem. B* **2005**, *109*, 22036–44.
- (41) Gaede, H. C.; Gawrisch, K. Lateral diffusion rates of lipid, water, and a hydrophobic drug in a multilamellar liposome. *Biophys. J.* **2003**, *85*, 1734–1740.
- (42) Geil, B.; Feiweier, T.; Pospiech, E. M.; Eisenblätter, J.; Fujara, F.; Winter, R. Relating structure and translational dynamics in aqueous dispersions of monoolein. *Chem. Phys. Lipids* **2000**, *106*, 115–126.

(43) Ghosh, R. Phosphorus-31 and deuterium NMR studies of structure and motion in bilayers of phosphatidylcholine and phosphatidylethanolamine. *Biochemistry* **1988**, *27*, 7750–7758.

(44) Roberts, M. F.; Redfield, A. G.; Mohanty, U. Phospholipid reorientation at the lipid/water interface measured by high resolution ³¹P field cycling NMR spectroscopy. *Biophys. J.* **2009**, *97*, 132–141.

(45) Dufourc, E. J.; Mayer, C.; Stohrer, J.; Althoff, G.; Kothe, G. Dynamics of phosphate head groups in biomembranes. Comprehensive analysis using phosphorus-31 nuclear magnetic resonance lineshape and relaxation time measurements. *Biophys. J.* **1992**, *61*, 42–57.

(46) Wang, T.; Cady, S. D.; Hong, M. NMR determination of protein partitioning into membrane domains with different curvatures and application to the influenza M2 peptide. *Biophys. J.* **2012**, *102*, 787–794.

(47) Schmidt, N. W.; Mishra, A.; Wang, J.; DeGrado, W. F.; Wong, G. C. Influenza virus A M2 protein generates negative Gaussian membrane curvature necessary for budding and scission. *J. Am. Chem. Soc.* **2013**, *135*, 13710–9.

(48) Rossmann, J. S.; Jing, X.; Leser, G. P.; Lamb, R. A. Influenza virus M2 protein mediates ESCRT-independent membrane scission. *Cell* **2010**, *142*, 902–913.

Supporting Information

Distinguishing Bicontinuous Lipid Cubic Phases from Isotropic Membrane Morphologies Using ^{31}P Solid-State NMR Spectroscopy

Yu Yang, Hongwei Yao and Mei Hong*

Department of Chemistry, Massachusetts Institute of Technology, 170 Albany Street, Cambridge, MA 02139

A. Geometric modeling of the three minimal surfaces

Three types of bicontinuous cubic phases have been found in lipids and surfactants: Pn3m (double diamond or D), Ia3d (gyroid or G), and Im3m (primitive or P). These minimal surfaces belong to the Triply Periodic Minimal Surfaces (TPMS) group, with translational symmetry in three principal directions. We built exact geometric models of the P, D and G minimal surfaces following the protocol of Klinowski¹⁻³, supplemented by Finch's corrections⁴⁻⁵. A unit cell of the TPMS consists of multiple fundamental patches, which is the basic repeating unit of the surface. We built the fundamental patch by mapping points from a complex plane Ω to the Cartesian coordinate system, then generate all other fundamental patches by reflection and rotation (**Tables S1-S3**). For P and G surfaces, 6 and 12 fundamental patches form a saddle, and 8 saddles form a unit cell. For the D surface, 6 fundamental patches form a unit cell. The procedure to construct these cubic-phase minimal surfaces can be represented by the following scheme:

$$\text{Complex plane } \Omega \xrightarrow{\text{elliptic integral}} \text{Fundamental patch} \xrightarrow{\text{symmetry}} \text{Saddle} \xrightarrow{\text{symmetry}} \text{Unit cell}$$

Scheme 1: Mathematical modeling of cubic-phase unit cells.

Primitive (Im3m) surface

The incomplete elliptic integral of the first kind is defined as:

$$\text{EllipticF}(\theta, m) = \int_0^{\sin\theta} \frac{d\tau}{\sqrt{1-\tau^2}\sqrt{1-m\tau^2}}. \quad (\text{S1})$$

The Cartesian coordinates of any points on the P fundamental patch can be expressed as^{3,5}:

$$\begin{cases} x = \frac{\kappa_p}{4} \operatorname{Re} \left\{ -i \cdot \operatorname{EllipticF} \left(\theta, \frac{1}{4} \right) + \operatorname{EllipticF} \left(\theta, \frac{3}{4} \right) \right\} \\ y = \frac{1}{2} - \kappa_p (2 - \sqrt{3}) \operatorname{Im} \left\{ \operatorname{EllipticF} \left[\phi, (2 - \sqrt{3})^4 \right] \right\} \\ z = 1 - \frac{\kappa_p}{4} \operatorname{Re} \left\{ i \cdot \operatorname{EllipticF} \left(\theta, \frac{1}{4} \right) + \operatorname{EllipticF} \left(\theta, \frac{3}{4} \right) \right\} \end{cases}, \quad (\text{S2})$$

where

$$\theta = \arcsin \left[\frac{2\sqrt{2}\omega}{\sqrt{\omega^4 + 4\omega^2 + 1}} \right], \quad \phi = \arcsin \left[(2 + \sqrt{3})\omega^2 \right]; \quad (\text{S3})$$

$\kappa_p = 2/\operatorname{EllipticK}(3/4)$ is a normalization constant, and

$$\operatorname{EllipticK}(m) = \operatorname{EllipticF}(\pi/2, m) \quad (\text{S4})$$

is the complete elliptic integral function of the first kind.

In Eqn. S3, $\omega = u + i \cdot v$ is a complex number in the plane Ω_p , where the real and imaginary parts u and v satisfy the condition

$$\begin{aligned} u \geq v \geq 0, \quad \left(u + \frac{\sqrt{2}}{2} \right)^2 + \left(v + \frac{\sqrt{2}}{2} \right)^2 \leq 2, \\ \text{or } u \geq -v \geq 0, \quad \left(u + \frac{\sqrt{2}}{2} \right)^2 + \left(v - \frac{\sqrt{2}}{2} \right)^2 \leq 2. \end{aligned}$$

In the plane Ω_p (**Fig. S1**), three distinct points can be found: $P: (\sqrt{3}-1)/\sqrt{2}$, $Q_1: (1+i)(\sqrt{2}-1)/\sqrt{2}$, and $Q_2: (1-i)(\sqrt{2}-1)/\sqrt{2}$.

All points on the Ω_p plane are mapped to the Cartesian coordinate system using Eqn. S2 to generate a fundamental patch F_1 of the P surface (**Fig. S1a-b**). Five additional patches are then generated by rotation and reflection of F_1 (**Table S1**), and these 6 patches form a saddle. 7 additional saddles are generated by reflections of the first saddle. These eight saddles combine to form a unit cell of the P surface. In **Fig. S1c**, a fundamental patch and a saddle are shown in red and blue, respectively.

Double diamond (Pn3m) surface

The Cartesian coordinates of points on the fundamental patch of the Pn3m surface are expressed in terms of $\operatorname{EllipticF}(\theta, m)$ as ⁴:

$$\begin{cases} x = \frac{1}{2} + \frac{\kappa_d}{4} \operatorname{Im} \left\{ -i \cdot \operatorname{EllipticF} \left(\theta, \frac{1}{4} \right) + \operatorname{EllipticF} \left(\theta, \frac{3}{4} \right) \right\} \\ y = \frac{1}{2} + \frac{\kappa_d}{4} \operatorname{Im} \left\{ i \cdot \operatorname{EllipticF} \left(\theta, \frac{1}{4} \right) + \operatorname{EllipticF} \left(\theta, \frac{3}{4} \right) \right\} \\ z = -\frac{1}{2} + \kappa_d (2 - \sqrt{3}) \operatorname{Re} \left\{ \operatorname{EllipticF} \left[\phi, (2 - \sqrt{3})^4 \right] \right\} \end{cases}, \quad (\text{S5})$$

where the normalization constant is $\kappa_d = 2/\operatorname{EllipticK}(1/4)$. For the double diamond surface, the complex plane Ω_d that corresponds to one fundamental patch satisfies:

$$\begin{aligned} & u \geq 0, v \geq 0, \left(u + \frac{\sqrt{2}}{2} \right)^2 + \left(v + \frac{\sqrt{2}}{2} \right)^2 \leq 2 \\ \text{or } & u \geq 0, v \leq 0, \left(u + \frac{\sqrt{2}}{2} \right)^2 + \left(v - \frac{\sqrt{2}}{2} \right)^2 \leq 2, \\ \text{or } & u \leq 0, v \leq 0, \left(u - \frac{\sqrt{2}}{2} \right)^2 + \left(v - \frac{\sqrt{2}}{2} \right)^2 \leq 2, \\ \text{or } & u \leq 0, v \geq 0, \left(u - \frac{\sqrt{2}}{2} \right)^2 + \left(v + \frac{\sqrt{2}}{2} \right)^2 \leq 2. \end{aligned}$$

Fig. S2a shows the Ω_d plane, on which four distinct points are marked: $P_1: (\sqrt{3}-1)/\sqrt{2}$, $P_2: i(\sqrt{3}-1)/\sqrt{2}$, $P_3: -(\sqrt{3}-1)/\sqrt{2}$, and $P_4: -i(\sqrt{3}-1)/\sqrt{2}$. Mapping this Ω_d domain onto the Cartesian coordinate system using Eqn. S5 gives rise to one fundamental patch of the D surface (**Fig. S2b**). 5 additional patches are generated by rotation and reflection of the first patch (**Table S2**). For example, rotation of the first fundamental patch F_1 (**Fig. S2b**) by 180° around the P_1P_4 vector gives rise to fundamental patch F_2 . A whole D surface unit is shown in **Fig. S2c**.

Gyroid (Ia3d) surface

The Cartesian coordinates of any points on the gyroid fundamental patch are expressed in terms of $\operatorname{EllipticF}(\theta, m)$ as^{2,5}

$$\begin{cases} x = -\frac{\kappa_g}{4} \operatorname{Re} \left\{ e^{i\theta} \left(\operatorname{EllipticF} \left(\theta, \frac{1}{4} \right) + i \cdot \operatorname{EllipticF} \left(\theta, \frac{3}{4} \right) \right) \right\} \\ y = \frac{1}{2} - \frac{\kappa_g}{4} \operatorname{Re} \left\{ e^{i\theta} \left(\operatorname{EllipticF} \left(\theta, \frac{1}{4} \right) - i \cdot \operatorname{EllipticF} \left(\theta, \frac{3}{4} \right) \right) \right\} \\ z = \frac{3}{4} + \kappa_g (2 - \sqrt{3}) \operatorname{Re} \left\{ e^{i\theta} \cdot \operatorname{EllipticF} \left[\phi, (2 - \sqrt{3})^4 \right] \right\} \end{cases}, \quad (\text{S6})$$

where $\vartheta = \text{arccot}(K'/K) \approx 38.01^\circ$ is the Bonnet angle, $K' = \text{EllipticK}(3/4)$, $K = \text{EllipticK}(1/4)$, and the normalization constant is $\kappa_g = \sqrt{1/K'^2 + 1/K^2}$.

For the gyroid surface, points (u, v) in the complex plane Ω_g satisfy the condition:

$$u \geq 0, v \geq 0, \left(u + \frac{\sqrt{2}}{2}\right)^2 + \left(v + \frac{\sqrt{2}}{2}\right)^2 \leq 2$$

In this Ω_g plane (**Fig. S3a**), 3 important points can be identified: O: 0; P₁: $(\sqrt{3}-1)/\sqrt{2}$ and P₂: $i(\sqrt{3}-1)/\sqrt{2}$. Mapping Ω_g onto the Cartesian coordinate system using Eqn. S6 gives rise to one fundamental patch (**Fig. S3b**), where O, P₁ and P₂ correspond to (0, 0.5, 0.75), (0, 0, 1) and (0.5, 0.5, 0.5), respectively, in the Cartesian coordinate system. 11 other fundamental patches are generated by rotation and reflection of F₁ (**Table S3**). These 12 patches form a saddle, and 7 additional saddles, generated by reflections of the first one, combine to form a unit cell (**Fig. S3c**) of the gyroid surface.

B. Simulation of ³¹P CSA lineshapes with other B₀ orientations

The orientation of the static magnetic field B₀ in the crystal frame can be described by polar and azimuthal angles θ and ϕ , respectively. When B₀ is parallel to the z-axis of the crystal frame, i.e. $\theta = 0$, the chemical shift calculation is particularly simple and gives the spectrum shown in **Fig. 1d** of the main text. Here we present simulated spectra for two additional orientations of B₀, to illustrate the diversity of these orientation-dependent lineshapes. Using the P (Im3m) surface as an example, when B₀ is oriented at $(\theta, \phi) = (54.7^\circ, 45^\circ)$, which is the point with the maximum surface area (**Fig. S4a**), the CSA spectrum (**Fig. S4b**) has enhanced intensity at the downfield edge (30 ppm) of the full chemical shift range compared to a lamellar powder spectrum. When B₀ is oriented at $(90^\circ, 45^\circ)$, the corresponding CSA lineshape (**Fig. S4c**) has the highest intensity at the upfield edge (-15 ppm) of the powder pattern and also has an enhanced intensity at about 15 ppm. When B₀ is along the x-axis ($\theta=90^\circ, \phi = 0^\circ$) and the y-axis ($\theta = 90^\circ, \phi = 90^\circ$), the chemical shift lineshape is identical to the spectrum obtained when B₀ is parallel to the z-axis (**Fig. 1d**). Finally, all three minimal surfaces give the same spectral lineshapes for the same B₀ orientations in their respective crystal frames.

Table S1. Generation of the primitive (Im3m) unit cell from the fundamental patch F_1 by symmetry operations. (x_1, y_1, z_1) denote the Cartesian coordinate of one point on the F_1 patch. S_1 is the first saddle generated from $F_1 - F_6$; (x_{s1}, y_{s1}, z_{s1}) denote the coordinate of a point on the saddle S_1 . S_1 to S_8 combine to form a unit cell.

Patch coordinate	X	Y	Z
F_1	x_1	y_1	z_1
F_2	$x_2 = x_1$	$y_2 = z_1$	$z_2 = y_1$
F_3	$x_3 = y_1$	$y_3 = z_1$	$z_3 = x_1$
F_4	$x_4 = z_1$	$y_4 = y_1$	$z_4 = x_1$
F_5	$x_5 = z_1$	$y_5 = x_1$	$z_5 = y_1$
F_6	$x_6 = y_1$	$y_6 = x_1$	$z_6 = z_1$
Saddle coordinate	X_s	Y_s	Z_s
S_1	x_{s1}	y_{s1}	z_{s1}
S_2	$x_{s2} = x_{s1}$	$y_{s2} = -y_{s1}$	$z_{s2} = z_{s1}$
S_3	$x_{s3} = x_{s1}$	$y_{s3} = -y_{s1}$	$z_{s3} = -z_{s1}$
S_4	$x_{s4} = x_{s1}$	$y_{s4} = y_{s1}$	$z_{s4} = -z_{s1}$
S_5	$x_{s5} = -x_{s1}$	$y_{s5} = y_{s1}$	$z_{s5} = -z_{s1}$
S_6	$x_{s6} = -x_{s1}$	$y_{s6} = y_{s1}$	$z_{s6} = z_{s1}$
S_7	$x_{s7} = -x_{s1}$	$y_{s7} = -y_{s1}$	$z_{s7} = z_{s1}$
S_8	$x_{s8} = -x_{s1}$	$y_{s8} = -y_{s1}$	$z_{s8} = -z_{s1}$

Table S2. Generation of the double diamond (Pn3m) unit cell from the fundamental patch F_1 by symmetry operations. (x_1, y_1, z_1) denote the Cartesian coordinate of one point on the F_1 patch. 6 patches combine to form a unit cell.

Patch coordinate	X	Y	Z
F_1	x_1	y_1	z_1
F_2	$x_2 = -x_1$	$y_2 = z_1 + 1$	$z_2 = y_1 - 1$
F_3	$x_3 = y_2 - 1$	$y_3 = x_2 + 1$	$z_3 = -z_2$
F_4	$x_4 = z_3 - 1$	$y_4 = -y_3$	$z_4 = x_3 + 1$
F_5	$x_5 = -x_4$	$y_5 = z_4 - 1$	$z_5 = y_4 + 1$
F_6	$x_6 = y_5 + 1$	$y_6 = x_5 - 1$	$z_6 = -z_5$

Table S3. Generation of a gyroid (Ia3d) unit cell from the fundamental patch F_1 by symmetry operations. (x_1, y_1, z_1) denote the Cartesian coordinate of one point on the F_1 patch. 12 patches comprise a saddle and 8 saddles comprise a unit cell.

Patch coordinate	X	Y	Z
F_1	x_1	y_1	z_1
F_2	$x_2 = -y_1 + 0.5$	$y_2 = x_1 + 0.5$	$z_2 = -z_1 + 1.5$
F_3	$x_3 = y_1$	$y_3 = z_1$	$z_3 = -x_1 + 1$
F_4	$x_4 = x_1 + 0.5$	$y_4 = -z_1 + 1.5$	$z_4 = y_1 + 0.5$
F_5	$x_5 = z_1$	$y_5 = -x_1 + 1$	$z_5 = -y_1 + 1$
F_6	$x_6 = -z_1 + 1.5$	$y_6 = y_1 + 0.5$	$z_6 = -x_1 + 0.5$
F_7	$x_7 = -x_1 + 1$	$y_7 = -y_1 + 1$	$z_7 = -z_1 + 1$
F_8	$x_8 = y_1 + 0.5$	$y_8 = -x_1 + 0.5$	$z_8 = z_1 - 0.5$
F_9	$x_9 = -y_1 + 1$	$y_9 = -z_1 + 1$	$z_9 = x_1$
F_{10}	$x_{10} = -x_1 + 0.5$	$y_{10} = z_1 - 0.5$	$z_{10} = -y_1 + 0.5$
F_{11}	$x_{11} = -z_1 + 1$	$y_{11} = x_1$	$z_{11} = y_1$
F_{12}	$x_{12} = z_1 - 0.5$	$y_{12} = -y_1 + 0.5$	$z_{12} = x_1 + 0.5$
Saddle coordinate	X_s	Y_s	Z_s
S_1	x_{s1}	y_{s1}	z_{s1}
S_2	$x_{s2} = -x_{s1}$	$y_{s2} = -y_{s1} + 1$	$z_{s2} = z_{s1}$
S_3	$x_{s3} = -x_{s1} + 1$	$y_{s3} = y_{s1} - 1$	$z_{s3} = z_{s1}$
S_4	$x_{s4} = x_{s1} - 1$	$y_{s4} = -y_{s1}$	$z_{s4} = z_{s1}$
S_5	$x_{s5} = x_{s1}$	$y_{s5} = -y_{s1} + 1$	$z_{s5} = z_{s1} - 1$
S_6	$x_{s6} = -x_{s1}$	$y_{s6} = y_{s1}$	$z_{s6} = z_{s1} - 1$
S_7	$x_{s7} = -x_{s1} + 1$	$y_{s7} = -y_{s1}$	$z_{s7} = z_{s1} - 1$
S_8	$x_{s8} = x_{s1} - 1$	$y_{s8} = y_{s1} - 1$	$z_{s8} = z_{s1} - 1$

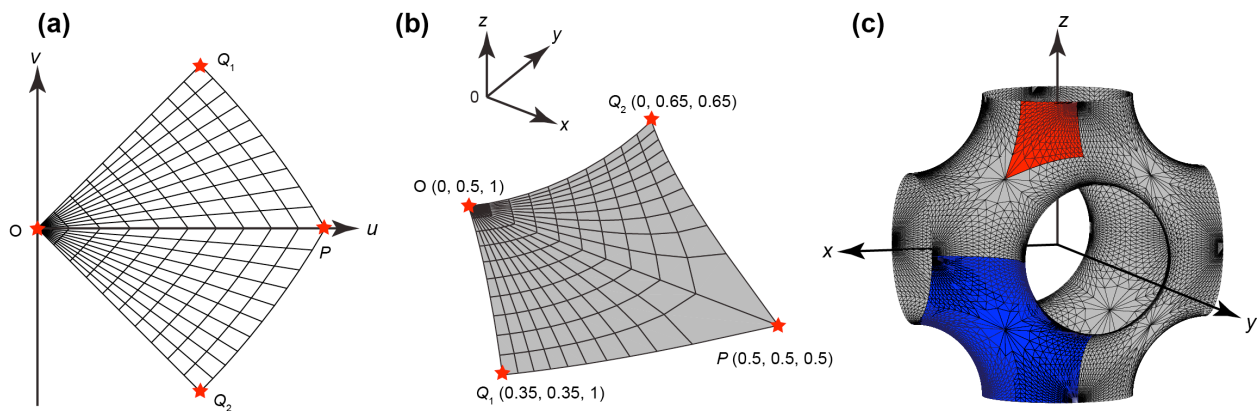


Figure S1. Mathematical modeling of the Im3m primitive surface. (a) The complex domain Ω_p . (b) One fundamental patch of the primitive surface in the Cartesian coordinate system. (c) One unit cell of the primitive surface. This unit contains 8 saddles, each of which contains 6 fundamental patches. Blue denotes one saddle and red denotes one patch.

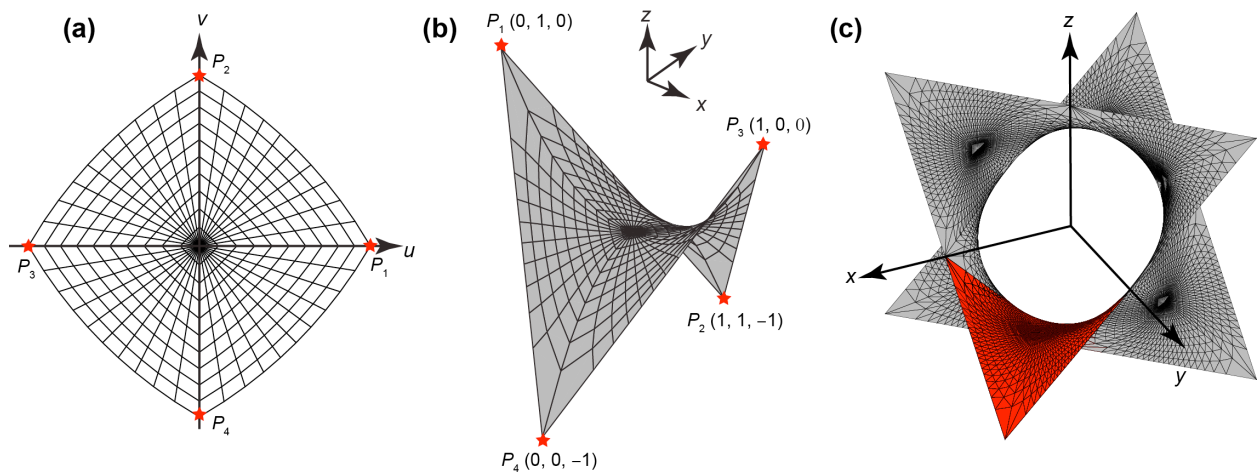


Figure S2. Mathematical modeling of the $Pn3m$ double diamond surface. (a) The complex domain Ω_d . (b) One patch of the double diamond surface in the Cartesian coordinate system. (c) One unit cell of the double diamond surface. Red color denotes one fundamental patch, six of which combine to form a unit.

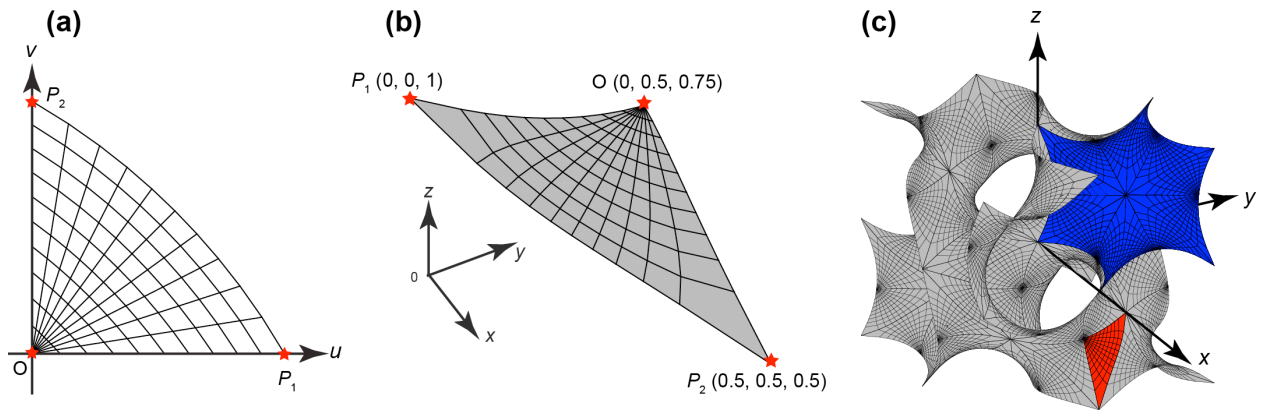


Figure S3. Mathematical modeling of the Ia3d gyroid surface. (a) The complex domain Ω_g . (b) One patch of the gyroid surface in the Cartesian coordinate system. (c) One unit cell of the gyroid surface. One unit contains 8 saddles, each of which contains 12 patches. Blue denotes one saddle and red denotes one patch.

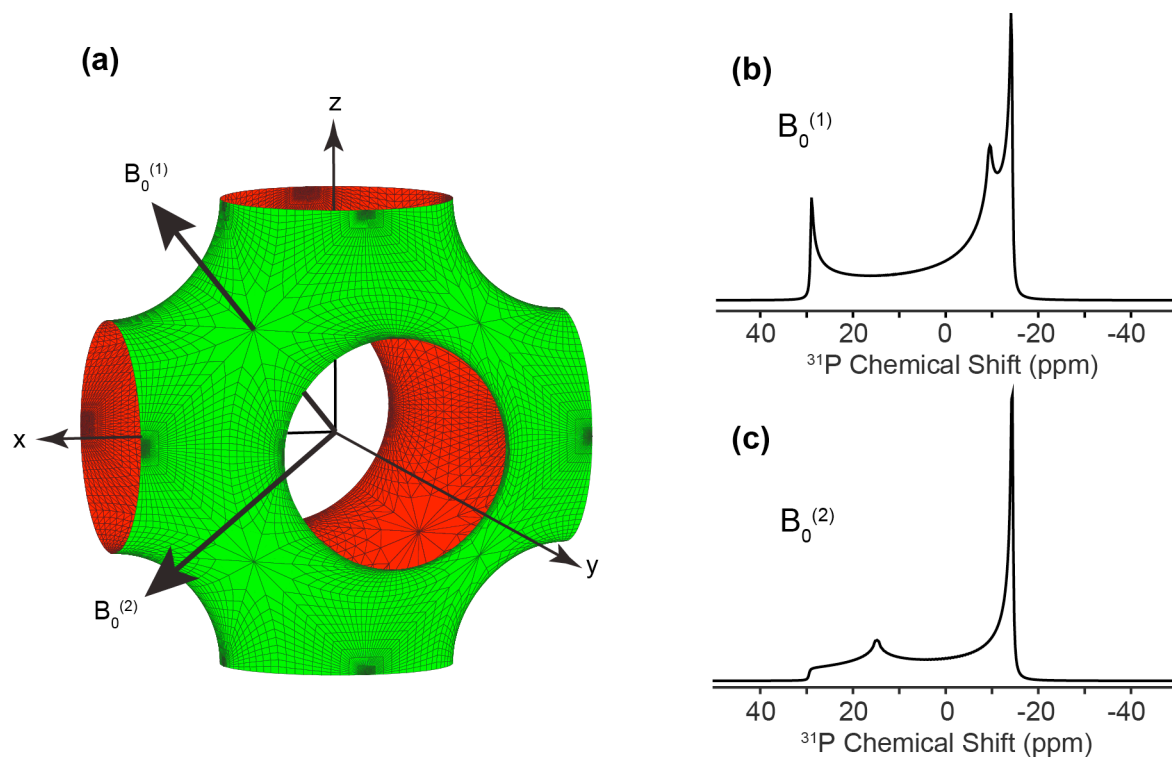


Figure S4. Simulated ^{31}P CSA lineshapes for two additional B_0 orientations in the crystal frame. (a) The unit cell of the primitive (Im3m) surface with the magnetic field at two different orientations. $B_0^{(1)}$ has $(\theta, \phi) = (54.7^\circ, 45^\circ)$, while $B_0^{(2)}$ has $(\theta, \phi) = (90^\circ, 45^\circ)$. (b) Simulated ^{31}P CSA lineshape for the $B_0^{(1)}$ orientation. (c) Simulated ^{31}P CSA lineshape for the $B_0^{(2)}$ orientation.

References

1. Gandy, P. J. F.; Cvijović, D.; Mackay, A. L.; Klinowski, J., Exact computation of the triply periodic D (diamond') minimal surface. *Chem. Phys. Lett.* **1999**, *314*, 543-551.
2. Gandy, P. J. F.; Klinowski, J., Exact computation of the triply periodic G (Gyroid') minimal surface. *Chem. Phys. Lett.* **2000**, *321*, 363-371.
3. Gandy, P. J. F.; Klinowski, J., Exact computation of the triply periodic Schwarz< i>P</i> minimal surface. *Chem. Phys. Lett.* **2000**, *322*, 579-586.
4. Finch, S. R. Computer algebra and elliptic functions. **2013**, <http://www.people.fas.harvard.edu/~sfinch/csolve/MinSrf.pdf>.
5. Finch, S. R. Partitioning problem. **2013**, <http://www.people.fas.harvard.edu/~sfinch/csolve/ge2.pdf>.